remote sensing

MDPI

Article

Mapping of Soil Liquefaction Associated with the 2021 Mw 7.4 Maduo (Madoi) Earthquake Based on the UAV Photogrammetry Technology

Wenxin Wang [1], Jing Liu-Zeng [1,2,*], Yanxiu Shao [1], Zijun Wang [1], Longfei Han [1], Xuwen Shen [1], Kexin Qin [1], Yunpeng Gao [1], Wenqian Yao [1], Guiming Hu [1], Xianyang Zeng [2], Xiaoli Liu [3], Wei Wang [2], Fengzhen Cui [1], Zhijun Liu [1], Jinyang Li [1] and Hongwei Tu [4]

[1] Institute of Surface-Earth System Science, School of Earth System Science, Tianjin University, Tianjin 300072, China
[2] State Key Laboratory of Earthquake Dynamics, Institute of Geology, China Earthquake Administration, Beijing 100029, China
[3] Key Laboratory of Earthquake Geodesy, Institute of Seismology, China Earthquake Administration, Wuhan 430071, China
[4] Earthquake Agency of Qinghai Province, Xining 810001, China
* Correspondence: liu_zeng@tju.edu.cn

Abstract: The 2021 Mw 7.4 Maduo (Madoi) earthquake that struck the northern Tibetan Plateau resulted in widespread coseismic deformation features, such as surface ruptures and soil liquefaction. By utilizing the unmanned aerial vehicle (UAV) photogrammetry technology, we accurately recognize and map 39,286 liquefaction sites within a 1.5 km wide zone along the coseismic surface rupture. We then systematically analyze the coseismic liquefaction distribution characteristics and the possible influencing factors. The coseismic liquefaction density remains on a higher level within 250 m from the surface rupture and decreases in a power law with the increasing distance. The amplification of the seismic waves in the vicinity of the rupture zone enhances the liquefaction effects near it. More than 90% of coseismic liquefaction occurs in the peak ground acceleration (PGA) > 0.50 g, and the liquefaction density is significantly higher in the region with seismic intensity > VIII. Combined with the sedimentary distribution along-strike of the surface rupture, the mapped liquefaction sites indicate that the differences in the sedimentary environments could cause more intense liquefaction on the western side of the epicenter, where loose Quaternary deposits are widely spread. The stronger coseismic liquefaction sites correspond to the Eling Lake section, the Yellow River floodplain, and the Heihe River floodplain, where the soil is mostly saturated with loose fine-grained sand and the groundwater level is high. Our results show that the massive liquefaction caused by the strong ground shaking during the Maduo (Madoi) earthquake was distributed as the specific local sedimentary environment and the groundwater level changed.

Keywords: soil liquefaction; Maduo (Madoi) earthquake; earthquake ground motion; sedimentary environment; UAV photogrammetry technology

Citation: Wang, W.; Liu-Zeng, J.; Shao, Y.; Wang, Z.; Han, L.; Shen, X.; Qin, K.; Gao, Y.; Yao, W.; Hu, G.; et al. Mapping of Soil Liquefaction Associated with the 2021 Mw 7.4 Maduo (Madoi) Earthquake Based on the UAV Photogrammetry Technology. *Remote Sens.* **2023**, *15*, 1032. https://doi.org/10.3390/rs15041032

Academic Editor: Salvatore Stramondo

Received: 26 December 2022
Revised: 16 January 2023
Accepted: 31 January 2023
Published: 14 February 2023

1. Introduction

At 02:04 (local time) on 22 May 2021, an Mw 7.4 earthquake struck the area of Maduo (Madoi) County (Qinghai Province, northwest China). According to the China Earthquake Network Center (CENC), the epicenter of the earthquake was located at 34.59°N, 98.34°E (https://www.cea-igp.ac.cn/kydt/278249.html, accessed on 22 May 2021) (Figure 1). The focal mechanism indicates that the earthquake was a dominantly left-lateral strike-slip on a near EW trending primary fault and a minor tensile component [1,2]. It was the strongest earthquake with the longest surface rupture in China after the 2008 Mw 7.9 Wenchuan earthquake, and another strong seismic event that has occurred on or near

the boundary faults of the Bayan Har Block in the last 20 years (Figure 1a). The Maduo (Madoi) earthquake (the following is abbreviated as Maduo earthquake) induced large-scale soil liquefaction that affected an area of up to ~10^3 km^2 [3,4]. The coseismic liquefaction caused the destruction of the grassland and the deterioration of important transportation infrastructures. Typical engineering damages in the earthquake-affected areas are often accompanied by liquefaction, particularly where bridges were severely damaged, such as the Yematan Bridge [4,5].

Seismic soil liquefaction is caused by a sudden rise of the pore water pressure in the soil under cyclic seismic loading. Consequently, the stress between the soil grains (inter-grain contact pressure and friction) decreases to zero, resulting in a near-liquid state of the soil [6,7] (Figure 2). This process mainly occurs in buried layers composed of water-saturated silt and fine sand [6–9]. After the onset of liquefaction, the pore water moves from the bottom to the top of the sediment profile under excess pore water pressure. The groundwater-saturated sand will break through the cover layer or spray out of the surface along the fissure, resulting in water spraying and sand bubbling and accumulating into mounds on the ground [6,7,10]. Widespread liquefaction-induced ground deformation and subsidence would cause intense damage to infrastructures and engineering structures in almost every strong earthquake, and well-known examples include the 1995 Kobe earthquake [11], the 1999 Chi-chi earthquake [12], the 2008 Wenchuan earthquake [8,13,14], the 2010–2011 Canterbury earthquake sequence [7,15–17], and the 2019 Ridgecrest earthquake sequence [18,19]. Coseismic soil liquefaction has therefore attracted increasing attention from seismologists and geologists in recent years.

In previous studies of coseismic liquefaction, post-earthquake investigations have been routinely conducted to document the features of coseismic liquefaction [8–10] and have provided insights into the processes related to them [8,17,18]. Yuan et al. [5] and Fu et al. [20] suggested that the intensity of the earthquake ground motion is an important influencing factor for determining whether the soil will liquefy or not [5,20]. In addition, the distance from the main fault/the epicenter is recognized as a major controlling factor for liquefaction [21]. Moreover, coseismic liquefaction often occurs in coastal, riverside, and lakeside areas, where high water tables and loose sediments are common features [16,18], indicating that the occurrence of coseismic liquefaction sites is not randomly distributed, but may be related to the sedimentary environment. Most of the studies on coseismic liquefaction were based on field investigations that usually imply large workloads and are easily affected by environmental conditions; therefore, exhaustive mapping of liquefaction sites is rare. In addition, the liquefaction characteristic information obtained in the previous studies is concentrated locally in areas where coseismic liquefaction occurs most intensively during a strong earthquake event. However, to determine the distribution characteristics and influencing factors of coseismic liquefaction more accurately, it is important to conduct a comprehensive investigation in the area that was affected by an earthquake. Therefore, a more effective, accurate, and intelligent method is required to conduct post-earthquake liquefaction investigations.

In this study, we focus on the Maduo Mw 7.4 earthquake that occurred in the high-elevation interior of the Tibet Plateau, with an average altitude of 4300 m, where the regional natural environment is harsh, and the source areas of the Yellow River are covered with marshes and dunes. Climate warming has significantly degraded the multi-year permafrost in the region. Since 1980, the regional seasonal permafrost thickness has gradually changed from 3.2 m to 2.8 m (Qinghai Meteorological Bureau), the seasonal thaw depth has increased, and the permafrost lower boundary elevation has risen. In addition, road access is limited in the study area. These rough conditions impede accurate field investigations of liquefaction. For such unfavorable conditions, the UAV photogrammetry technology is an excellent tool for supporting field surveys on coseismic liquefaction. The technology obtains image sets through motion cameras, and it only requires digital image sets with certain overlap to establish high-resolution Digital Orthophoto Maps (DOMs) and Digital Elevation Models (DEMs) rapidly in order to build the original 3D appearance of the target objects in the

computer [22–25]. Several studies have proven the feasibility of the UAV photogrammetry in presenting the characteristics of post-earthquake liquefaction [26,27].

Here, based on the orthophotos within a 1.5 km wide zone along coseismic surface rupture collected through the UAV photogrammetry technology, we perform the manual identification and fine mapping of liquefaction. Our detailed and systematic survey focusing on the liquefaction features triggered by the Maduo earthquake aims to: (1) present a methodological approach for precisely locating and quantitatively documenting the liquefaction manifestations; (2) decipher the relationship between the occurrence of liquefaction and the distance from and along the main fault, the peak ground acceleration (PGA) and seismic intensity, in order to reveal the relevance between the liquefaction, seismic ground motion, and kinematics of the earthquake rupture; and (3) compare the spatial distribution of liquefaction with the depositional environment distribution in the coseismic area, thus exploring the link between the liquefaction distribution and sedimentary environment.

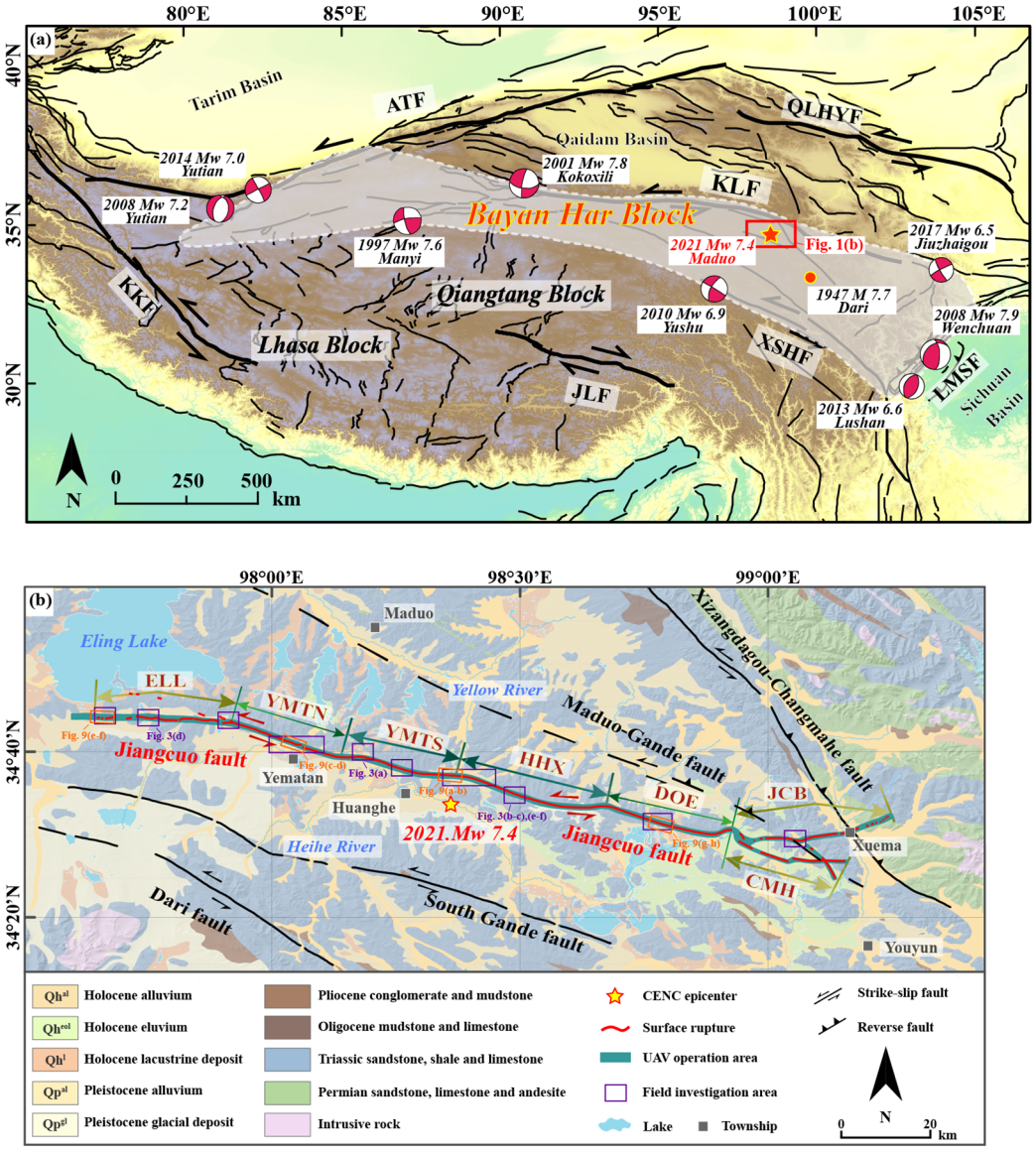

Figure 1. *Cont.*

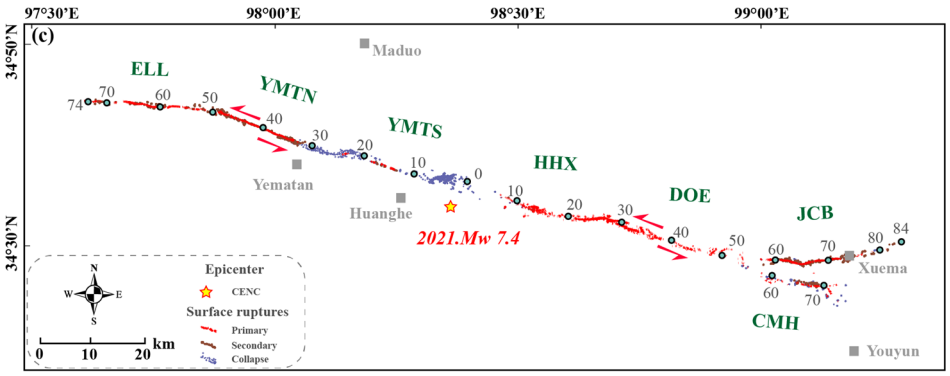

Figure 1. (**a**) Active tectonics and historical earthquakes (in the past 25 years) around the Bayan Har Block. Fault data are modified by Tapponnier et al. [28], Rui et al. [29] and Burchfiel et al. [30]. Mw $\geq$ 6.5 earthquakes that have occurred at the boundary of the Bayan Har Block since the turn of the century include: the 2001 Mw 7.8 Kokoxili earthquake [31], the 2008 Mw 7.9 Wenchuan earthquake [32], the 2010 Mw 6.9 Yushu earthquake [33], the 2013 Mw 6.6 Lushan earthquake [34], the 2008 Mw 7.0 and 2014 Mw 7.2 Yutian earthquake [35,36], and the 2017 Mw 6.5 Jiuzhaigou earthquake [37]. Abbreviations for active faults: ATF, Altyn Tagh fault; QLHYF, Qilian-haiyuan fault; KLF, Kunlun fault; LMSF, Longmenshan fault; XSHF, Xianshuihe fault; JLF, Jiali fault; KKF, Karakoram fault. Small red box is location of Figure 1b. (**b**) Geologic and tectonic setting of the 2021 Mw 7.4 Maduo earthquake. Geological data are from the public geological map (1:500,000). Active faults adapted from Tapponnier et al. [38], Pan et al. [2] and Ren et al. [39]. Seismic data are from China Earthquake Networks Center (https://www.cea-igp.ac.cn/kydt/278249.html, accessed on 22 May 2021). Small orange boxs are location of Figure 9. (**c**) Coseismic surface ruptures of the 2021 Mw 7.4 Maduo earthquake. Databases are obtained from post-earthquake identification and mapping based on the UAV photogrammetry technology (modified by Liu-Zeng et al. [1]).

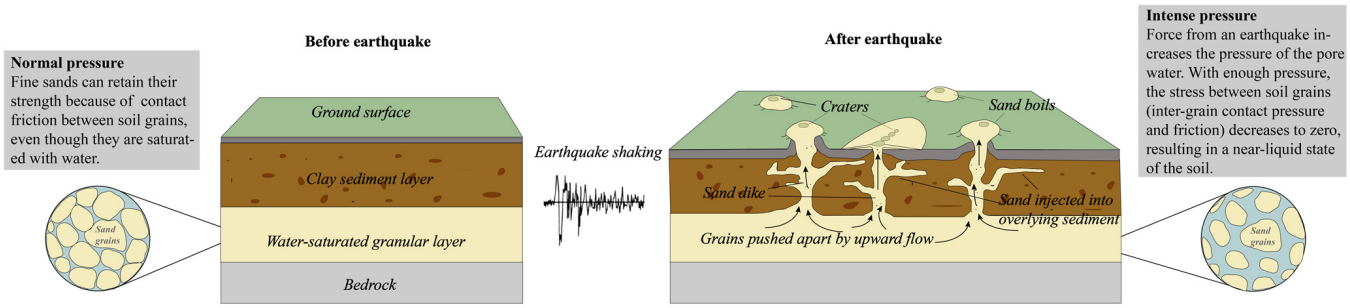

Figure 2. Schematic diagram illustrating the conceptual model of soil liquefaction during an earthquake. This process mainly occurs in buried layers composed of water-saturated silt and fine sand [6–9]. Under excess pore water pressure caused by cyclic seismic loading, the groundwater-saturated sand will break through the cover layer or spray out the surface along the fissure, resulting in water spraying and sand bubbling and accumulating into mounds on the ground [6,7,10].

2. Geological and Tectonic Setting

The Mw 7.4 Maduo earthquake occurred within the Bayan Har Block in the north-central Tibetan Plateau. A series of major active boundary faults, including the Kunlun, Xianshuihe, Altyn Tagh, and Longmen Shan faults, controls the current movement of the Bayan Har Block [28–30], as shown in Figure 1a. Several strong earthquakes have ruptured along these boundary faults in this century, such as the 2001 Mw 7.8 Kokoxili earthquake [31], the 2008 Mw 7.9 Wenchuan earthquake [32], and the 2008 Mw 7.0 and 2014 Mw 7.2 Yutian earthquakes [35,36]. These large, frequent, Mw $\geq$ 6.0 earthquakes in the past ~20 years demonstrate that the Bayan Har Block is one of the most seismically active crustal blocks in China.

The coseismic surface rupture develops along the Jiangcuo fault during this earthquake event and has a total length of ~158 km (Figure 1b,c). Based on the change in the fault orientation and step-overs, it can be divided into seven sections, named, from west to east: the Eling Lake (ELL), Yematan northern (YMTN), Yematan southern (YMTS), Huanghexiang (HHX), Dongcaoalong Lake (DOE), Changmahe (CMH), and Jiangcuo branch (JCB) sections (Figure 1b,c). Other major active faults in our study area include the East Kunlun fault zone in the north, the Xizangdagou-Changmahe fault, the Maduo-Gande fault and the Jiangcuo fault in the central part, and the South Gande fault and the Dari fault in the south [2,38,39] (Figure 1b).

As the source region of the Yellow River, the seismically affected area comprises abundant rivers and lakes. The low relief mountains and valleys of the region bear the imprint of glaciation, such as U-shaped valleys and moraines. Extensive alluvial fans are located at the valley margins, with several terraces outside the contemporary floodplain, and they consist mainly of silty sands and silts with occasional coarse sands and gravels. The geology of the study area is dominated by terrestrial Mesozoic to Cenozoic sedimentary rocks, whereas Quaternary sediments are widely developed in the Yellow River and its tributaries basin (Figure 1b). The moletracks of the coseismic surface ruptures are most prominent in the bedrock hillslopes and soil liquefaction is best demonstrated in the regions dominated by Quaternary sediments [40].

3. Data Acquisition Methods

3.1. Field Investigation of Liquefaction

We conducted our field investigations and detailed observation records immediately after the Maduo earthquake, which reduced the post-earthquake modification of the liquefaction features through natural erosion processes or wild animal and human activities. The field work lasted between 24 May and 5 June 2021, and the purple boxes in Figure 1b show the area we investigated. In the field, we recorded the characteristics of the liquefaction phenomena, including the liquefaction type, shape, dimension, grain size, and color. Then, the second field investigation was conducted between 26 September and 9 October 2021. The main task of this survey was to compare whether the locations of the liquefaction identified manually on the UAV images were consistent with the locations of the field liquefaction in order to verify our identification results.

3.2. UAV Image Acquisition and Liquefaction Identification

In addition to the field investigation, we obtained the Digital Orthophoto Maps (DOMs) of a 1.5 km wide-swath region for ~180 km length along the surface ruptures based on the UAV images acquired between 24 May and 5 June 2021. The accurate identification and fine mapping of liquefaction phenomena were completed on the DOMs.

We used the CW-15 electric VTOL (vertical take-off and landing) hybrid wing (two fixed wings and four rotors) UAV system equipped with a 42-million-pixel SLR camera and GPS module. Initially, we identified and located the surface rupture by the InSAR data [41] and field observations, and the surface rupture was used as the aerial photography operation centerline. In addition, the InSAR range-offset maps provided an excellent guide for planning the airborne data acquisition. We designed a photogrammetric corridor that was 180 km in length and covered a 1.5 km wide-swath region of the centerline, and appropriately widened the aerial photography range in the epicenter section. Subsequently, we imported the designed photogrammetric corridor into the CWCommder flight control platform in the KMZ file format, which automatically sets up the aerial photography area and generates the aerial survey line. The forward and side overlap ratio of the aerial photos were 80%. To improve the accuracy of the absolute position of the aerial photos, the UAV Pos data was calibrated by the Real-Time Kinematic (RTK) ground base stations and Continuously Operating Reference Stations (CORS) data. Every time the aerial photogrammetry data of a sortie was obtained, the position calculation software was used to immediately solve the UAV Pos data, RTK base station position data, and CORS

station data in order to obtain the precise position information of the aerial photographs, including the latitude and longitude coordinates, elevation, positioning accuracy, and UAV flighting parameters.

At present, the most frequently used solution for the UAV image sequence process is based on the structure from the motion (SfM) algorithm [24,42]. The typical SfM process workflows are published in Turner et al. [43], Ajayi et al. [44], and Giordan et al. [45]. The number of software that can obtain photo sequences and the available process data has gradually increased in the past few years. We used the semi-automated commercial software Agisoft PhotoScan^{TM} in our study. The operation process can be divided into the following steps: (1) Pre-process the photos, eliminate the photos with poor imaging, and import the photos with high quality into the software; (2) obtain the homonymic features between photos, recover the relative position and angle of the cameras during photography, reconstruct the 3D scene structure, and generate the dense point cloud data; (3) use the coordinate position of the ground control points for absolute correction and convert the 3D coordinate of the point cloud to the real space coordinate system; (4) generate grids and textures, and obtain the data, such as point clouds and DOMs with the spatial geographic coordinates [46]. The resolution of the final images mostly vary between 3–6 cm/pixel.

Then, we applied the GIS software to vectorize the liquefaction phenomena and counted the number of the liquefaction sites. We first circled the liquefaction area on the DOMs (as shown in Figure 3), and then validated our identification results with the field liquefaction sites in the field. Through continuous and repeated checking, we summarized the performance characteristics of liquefaction on the images and unified the identification standard. In addition, we counted the liquefaction sites based on the following rules: A single sand boil is counted as one liquefaction site (as shown in Figure 3a,c); for the sand fissures, if the sandblasting area is continuous, it will be counted as one liquefaction site; if the sandblasting area is interrupted, it will be counted separately (as shown in Figure 3b).

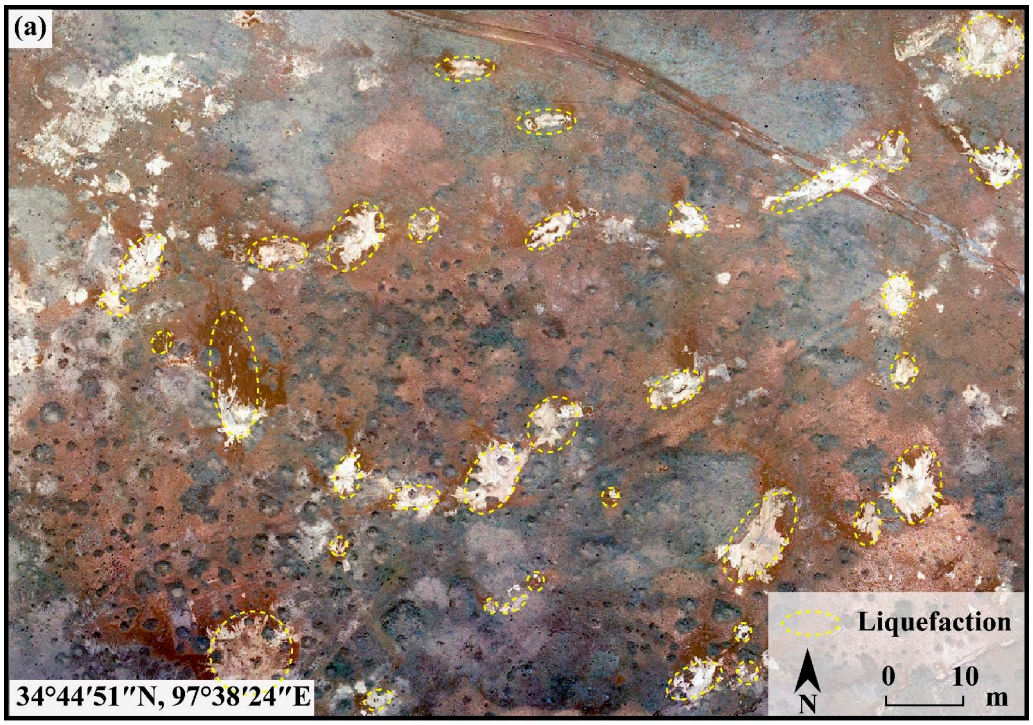

Figure 3. *Cont.*

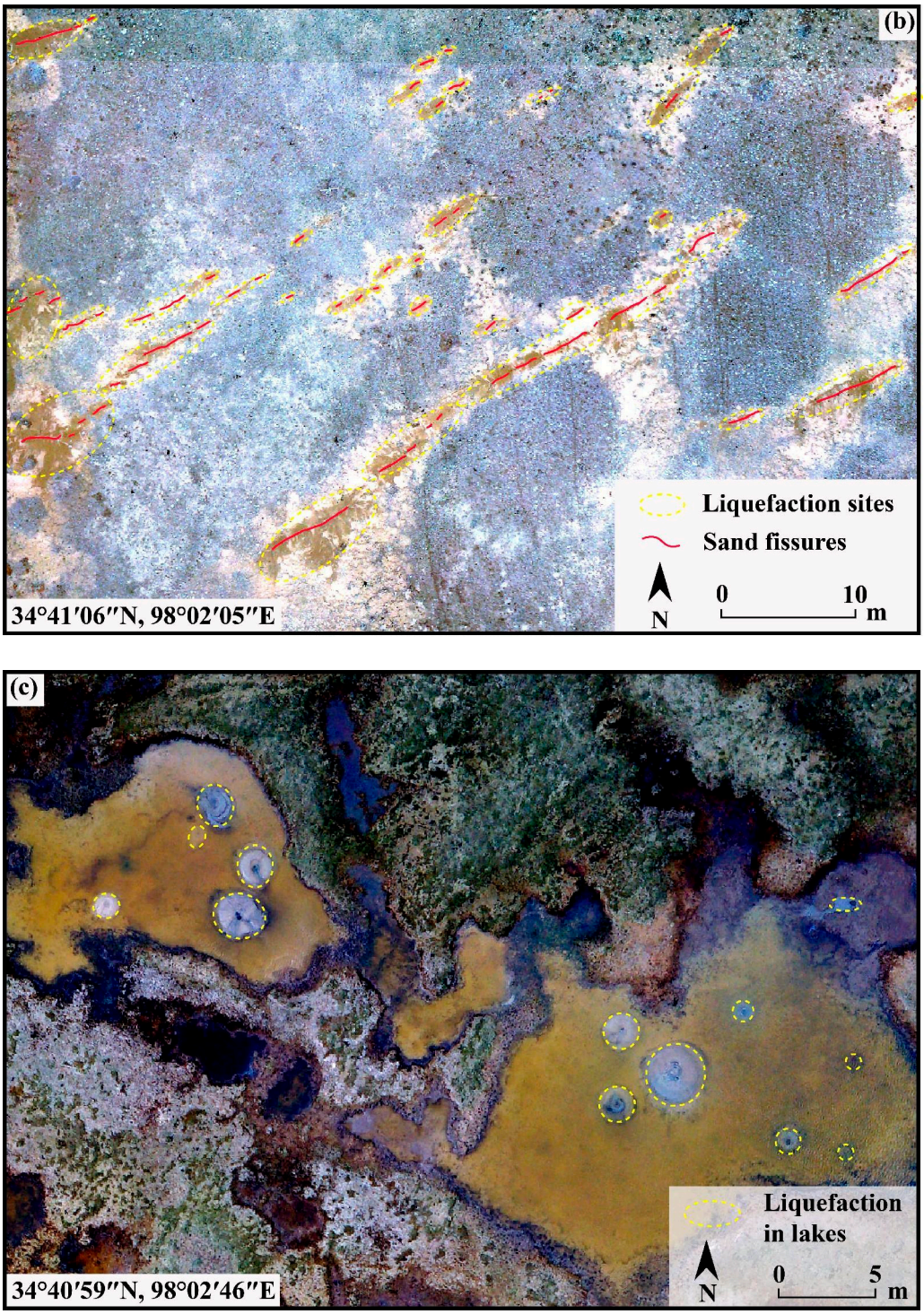

Figure 3. Some examples of soil liquefaction phenomena interpretation based on high-resolution DOMs.

4. Results

The liquefaction induced by the Maduo earthquake is mainly manifested by three types of phenomena: Sand boils, sand fissures, and lateral spreading (Figure 4). A single sand boil is predominantly circular or elliptical in shape and the ground fracture ejection liquefied materials are distributed in linear and beaded shapes. The size of the liquefaction area varies, and most of them are between 20 cm and 5 m in length, while their width ranges between 20 cm and 1.5 m. The size of the sandblast hole ranges between 4 cm × 2 cm and 90 cm × 50 cm. The thickness of the sand layer near the sandblast hole can reach 20 cm,

and the edge part is generally thin (ca. 3–5 cm). The material composition of liquefaction is mainly fine sand, and the color is mostly yellow, brown, or gray.

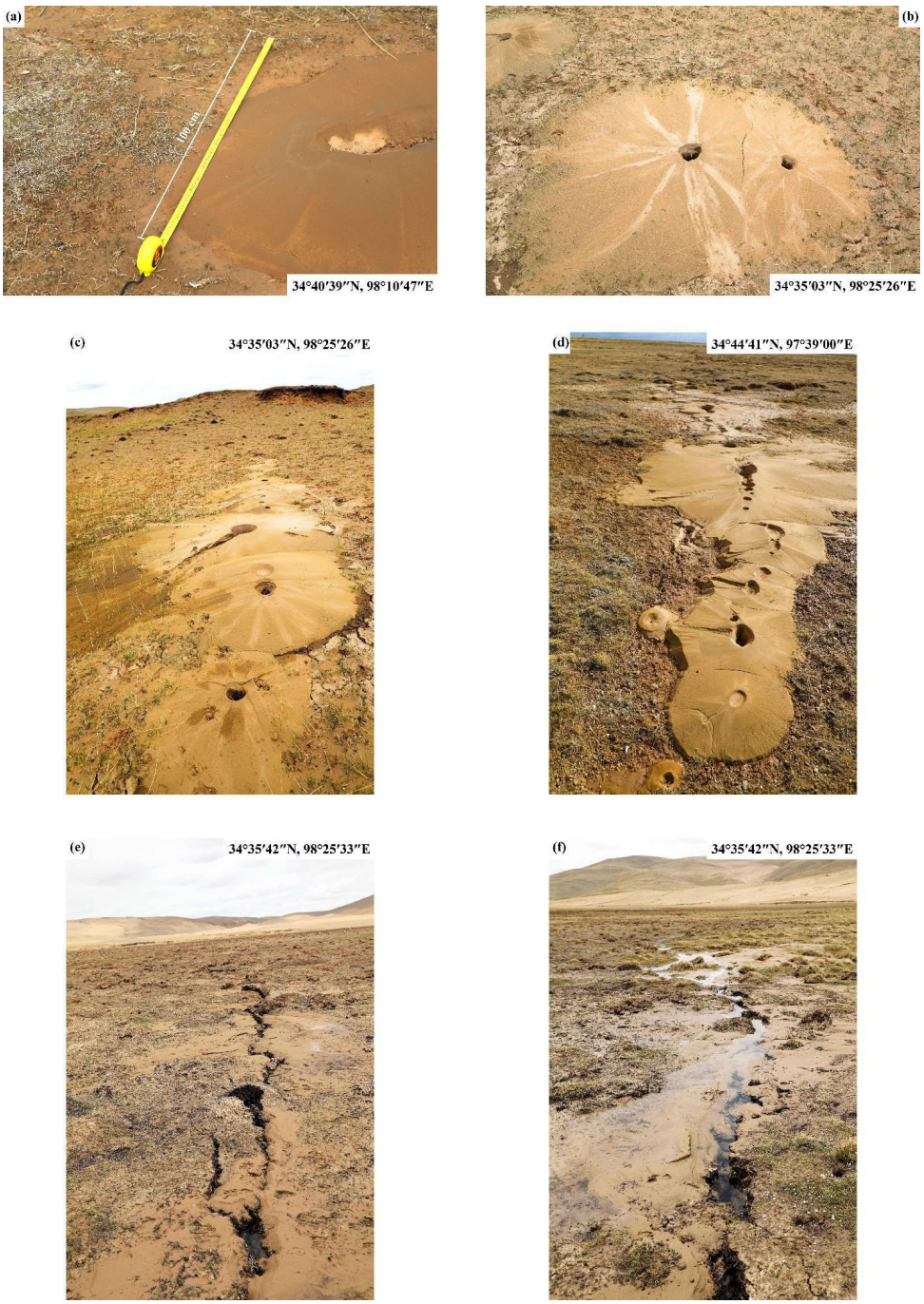

Figure 4. Soil liquefaction phenomena in the field.

Figure 3 shows the high-resolution orthophotos obtained from the UAV photogrammetry technology. The size and color of the liquefaction is well visualized by the images and even the liquefaction occurring in the lake can be identified. In addition, during the process of manual recognition, we repeatedly compared the original photos taken by the UAV and the DOMs, which further ensures the accuracy of our manual recognition results. Figure 5a shows the results of the manual interpretation of the liquefaction phenomena, and the yellow points are the manually identified liquefaction sites. Thus, we obtained an extensive coseismic liquefaction dataset with a total amount of 39,286 liquefaction phenomena sites.

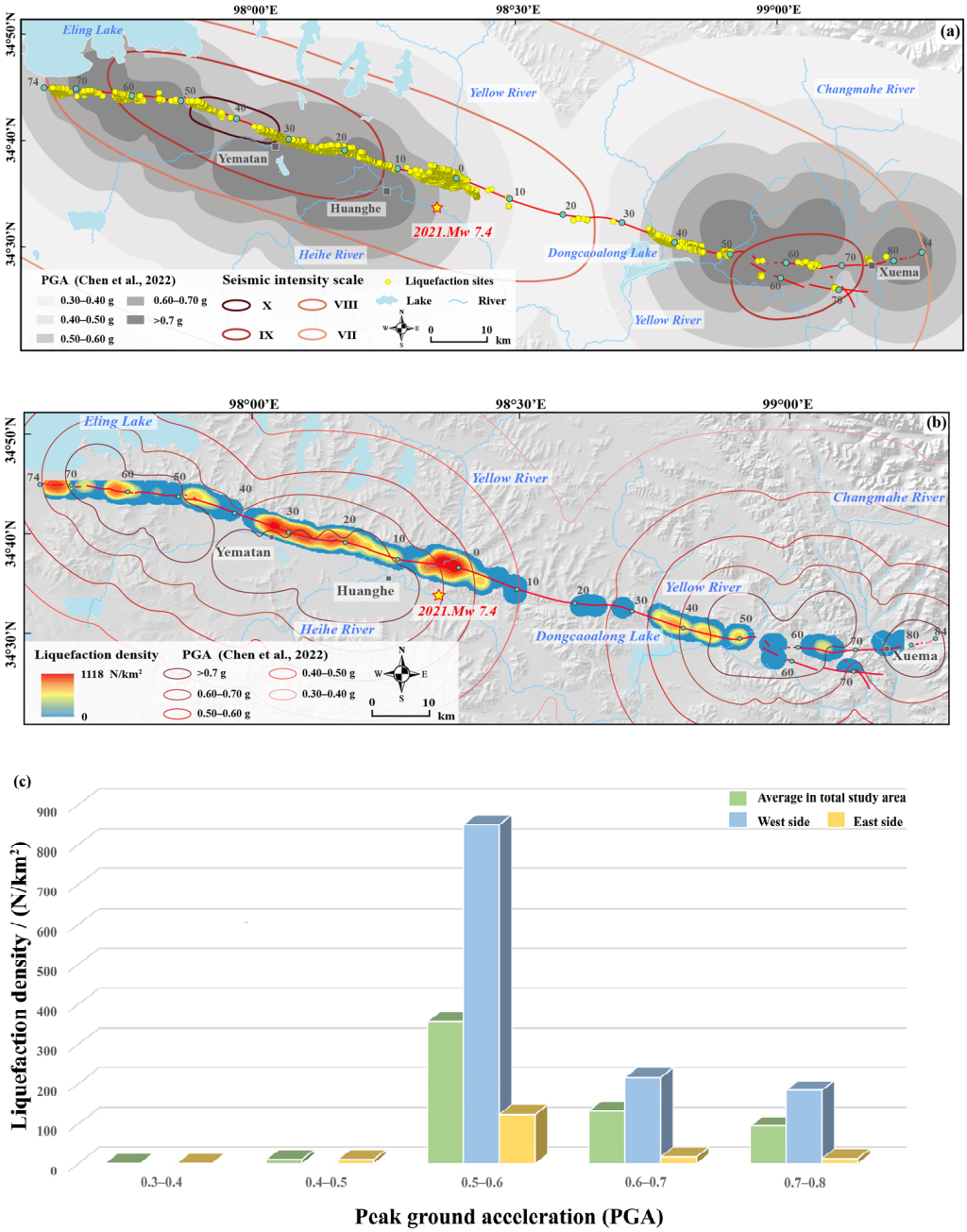

Figure 5. Coseismic soil liquefaction distribution map. (**a**) The yellow points are the coseismic soil liquefaction datasets interpreted based on UAV images, the peak ground acceleration (PGA) data are obtained from Chen et al. [47], and seismic intensity data are obtained from Ministry of Emergency Management of the People's Republic of China (https://www.mem.gov.cn/xw/yjglbgzdt/202105/t20210528_386251.shtml, accessed on 28 May 2021). (**b**) Density distribution map of coseismic soil liquefaction. (**c**) Liquefaction density in different PGA regions of the Maduo Mw 7.4 earthquake.

4.1. Liquefaction Distribution Versus the Peak Ground Acceleration (PGA)

Soil liquefaction results from pore pressure build up due to cyclic loading caused by passing seismic waves, and the coseismic liquefaction process is highly sensitive to repetitive cycles of surface wave shear strain [6]. Seismic ground motion is thus one of the most important factors controlling the occurrence and distribution of liquefaction effects, and the distribution of soil liquefaction is sometimes compared with the peak ground acceleration (PGA) and seismic intensity [5,6,13]. Chen et al. [47] applied a novel method that consisted of array technology (back projection), ground-motion prediction equations,

and site corrections to estimate the ground motion for each site of the 2021 Mw 7.4 Maduo earthquake. Based on the area covered by the UAV photographic corridor in this study, we selected five gradient peak ground accelerations (PGA) (0.30–0.40 g, 0.40–0.50 g, 0.50–0.60 g, 0.60–0.70 g, and >0.70 g) from the results of Chen et al. [47] (Figure 5). In the study area, nearly 99% of the coseismic liquefaction occurred in the PGA > 0.50 g. The highest liquefaction density was in the 0.50–0.60 g range, reaching 357 N/km^2. The liquefaction densities in the 0.60–0.70 g and >0.70 g ranges were 132 N/km^2 and 95 N/km^2, respectively.

We performed a density analysis of the liquefaction distribution using the GIS software. The density distribution map in Figure 5b shows that the liquefaction distribution in the east and west of the epicenter is significantly different. The amount of liquefaction phenomena on the western side was 34,468, accounting for 86.87%, which was much higher than that in the east of the epicenter. The PGA covered in the west of the epicenter only included 0.50–0.60 g, 0.60–0.70 g, and >0.70 g, and the liquefaction densities in the three ranges were 851 N/km^2, 216 N/km^2, and 185 N/km^2, respectively. The liquefaction in the east of the epicenter was more distributed in 0.50–0.60 g, 0.60–0.70 g, and >0.70 g ranges, with densities of 357 N/km^2, 132 N/km^2, and 95 N/km^2, respectively, whereas liquefaction in the 0.30–0.40 g and 0.40–0.50 g ranges was comparably rare (Figure 5c).

4.2. Liquefaction Distribution along the Surface Rupture

In the UAV photographic gallery, we investigated the distribution characteristics of the liquefaction along the surface rupture. Centering on the location of the epicenter determined by the CENC (34.59°N, 98.34°E), the liquefaction density distribution was calculated every 5 km along the rupture, extending 74 km to the west and 84 km to the east. Figure 6 shows our statistical results.

In the west of the epicenter, the liquefaction density was the highest in the 30–35 km section (W30–35), reaching 992 N/km^2, while the liquefaction densities in the W35–40 and W50–55 sections were extremely low, with only 1 N/km^2 and 7 N/km^2, respectively. The liquefaction densities were significantly higher than the other regions in the W0–5, W20–35, and W70–74 sections. Within the east of the epicenter, a certain scale of liquefaction distribution occurred in the 0–5 km (E0–5) and 35–50 km (E35–50) sections, with the highest liquefaction density of 177 N/km^2 in E35–40. Only sporadic or no liquefaction was recognized in the other sections.

We also compared the liquefaction densities between the north and south sides of the surface rupture (Figure 6b). In the west of the epicenter, the liquefaction distribution on the southern side was concentrated in the W0–5 and W20–35 sections. The maximum liquefaction amounts occurred in W30–35 with a density of 1450 N/km^2, while liquefaction was absent in W35–40. On the northern side, the liquefaction was mainly concentrated in the W0–5, W20–35, and W70–74 sections. The maximum liquefaction density occurred in W0–5 with 812 N/km^2, and the minimum liquefaction density occurred in W35–40 with 2 N/km^2. In the east of the epicenter, the liquefaction was concentrated in the E0–5 and E35–50 sections, both on the rupture's southern and northern sides. The maximum liquefaction density was 184 N/km^2 on the northern side in E0–5 and 220 N/km^2 on the southern side in E35–40.

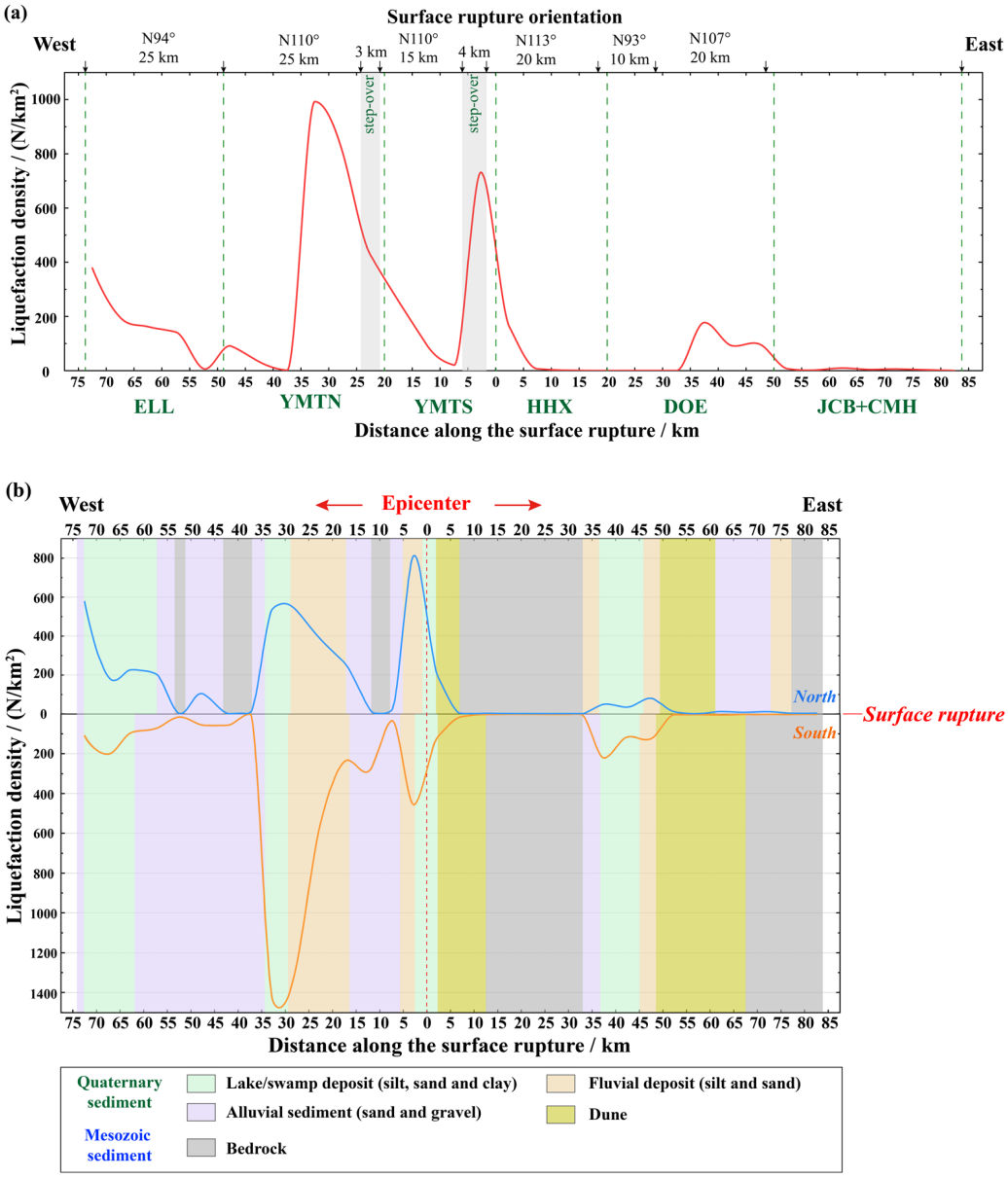

Figure 6. (**a**) Variation of soil liquefaction density along the surface rupture. The orientation information of surface ruptures is obtained from Liu-Zeng et al. [1]. (**b**) Difference of soil liquefaction density between the north and south sides of the surfae rupture.

4.3. Liquefaction Density Decay away from the Surface Rupture

We quantified the distribution trend of the coseismic liquefaction with the distance from the surface rupture in the study area. We measured the shortest distance between each liquefaction phenomenon and the rupture and found that the liquefaction density defined an inverse power law with the distance from the rupture. We fit these liquefaction distributions with the relationship proposed by Powers and Jordan [48] and Rodriguez Padilla et al. [49], where the decay with the distance from the surface rupture is defined by the density at the rupture ν_o, a parameter representing the distance between the origin and a break in scaling d, the sharpness of the corner m, and γ, which is the slope of the decay at distance $x >> d$:

$$\nu(x) = \nu_0 \left(\frac{d^m}{|x^m| + d^m} \right)^{\frac{\gamma}{m}} \quad (1)$$

We used an ensemble sampler for the Markov chain Monte Carlo to fit Equation (1) to our datasets, assuming that the $v(x)$ within each bin samples a Poisson distribution. We insert $m = 2$, as the quality of the fits do not vary significantly with the corner sharpness.

Figure 7a shows the density decay trend of all the liquefaction in the study area, where d was ~250 m. This implied that the liquefaction density remains at nearly a constant level within 250 m from the surface rupture, with a liquefaction density of ~339 N/km^2. Then, further away from the rupture, the liquefaction density decreased with the increasing distance in the power law, and the liquefaction density at the greatest distance from the rupture was two orders of magnitude lower. We further analyzed the liquefaction distribution to the west and east of the epicenter (Figure 7b,c). In the region west of the epicenter, d was 245 m. In the near field (d < 245 m), the liquefaction density was ~947 N/km^2, and at the greatest distance from the rupture, the liquefaction density was ~30 N/km^2 (Figure 7b). On the east side, the liquefaction density fluctuated with the increasing distance from the rupture, but remained at ~37 N/km^2, which was one order of magnitude less than that west of the epicenter. The liquefaction density quickly decayed for d > 839 m and the liquefaction distribution was almost absent at the greatest distance from the rupture (Figure 7c).

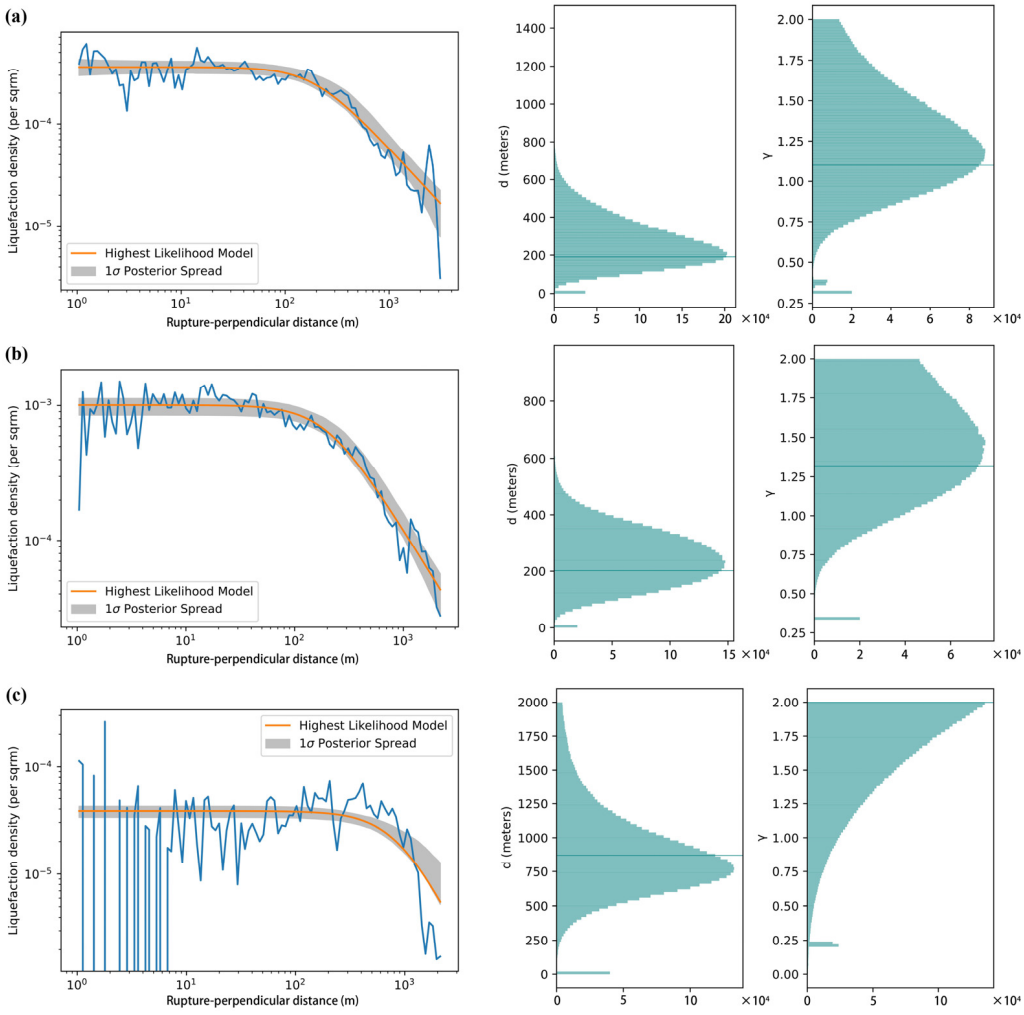

Figure 7. Variation of liquefaction density with increasing distance from the surface rupture in several sections. (**a**) Total study area, (**b**) west of the epicenter, and (**c**) east of the epicenter. The blue line shows the actual trend of liquefaction density with increasing distance from the rupture, the orange line shows the best-fit curve of the trend of liquefaction density, and the gray bar is the 1σ error. d represents the distance from the surface rupture when the liquefaction density begins to decay, γ is the slope of the decay at distance $x >> d$.

4.4. Liquefaction Distribution and Sedimentary Environments

The liquefaction process mainly occurs in buried layers composed of water-saturated silt and fine sand [6–9]. Previous studies have shown that the distribution of coseismic liquefaction is closely related to the local hydrological and sedimentary conditions [16,18]. We compared the liquefaction density with the type of sediments exposed on the surface within a 1.5 km wide swath of the surface rupture. In the region west of the epicenter, the rupture cut across the Holocene alluvium, diluvium, and lacustrine deposits. In contrast, more Mesozoic bedrocks are exposed in the east of the epicenter, with rare Quaternary deposits (Figure 6b). We compared the liquefaction distribution in different sedimentary environments and found that the vast majority of the liquefaction occurred in the lake/swamp deposits and fluvial deposits, accounting for 54.78% and 32.95%, respectively (Figure 8). Increased liquefaction was recognized near the floodplain and meanders of the Yellow River and the Heihe River, as well as the Eling Lake and Dongcaoalong Lake, such as the W0–5, W20–35, W70–75, E0–5 and E35–50 sections. In contrast, liquefaction rarely occurred in the dune regions and was almost absent on the bedrocks, which is understandable (Figure 6b).

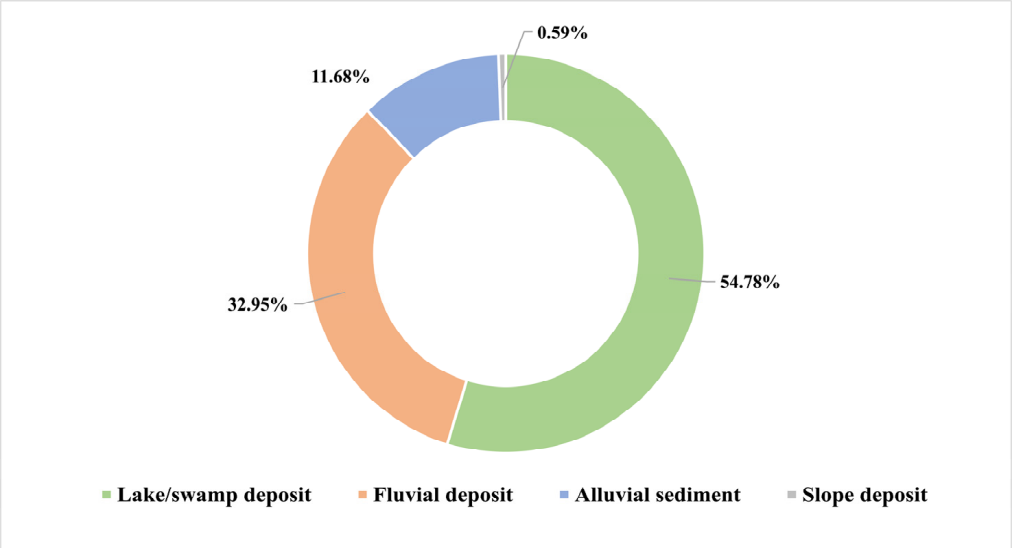

Figure 8. Liquefaction distribution in different Quaternary sediments.

We selected specific sections with the densest liquefaction distribution to conduct the density distribution map statistics, including the W0–5, W30–35, W70–75, and E35–40 sections, and conducted fine mappings of the sediment distribution of these sections (Figure 9). These sections are dominated by fluvial deposits and lake/swamp sediments and the liquefaction was concentrated in these two types of sediments. A smaller amount of liquefaction also occurred on the alluvial fans, which were situated close to river channels or lakes. However, the liquefaction distribution on the bedrocks and Quaternary deposits far from the rivers/lakes was lacking, exemplifying that a shallow groundwater level also has an influence on the onset of liquefaction.

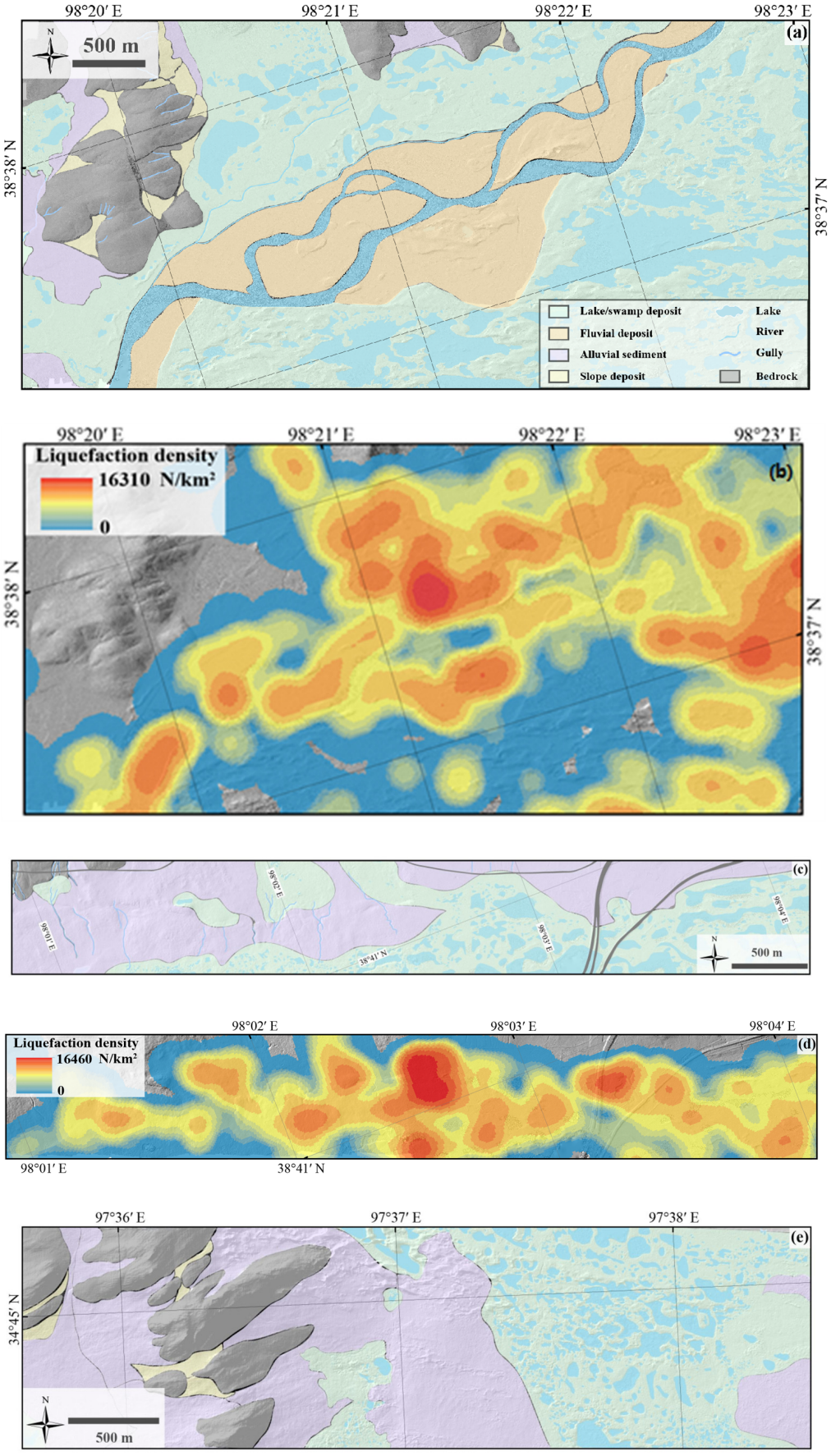

Figure 9. *Cont.*

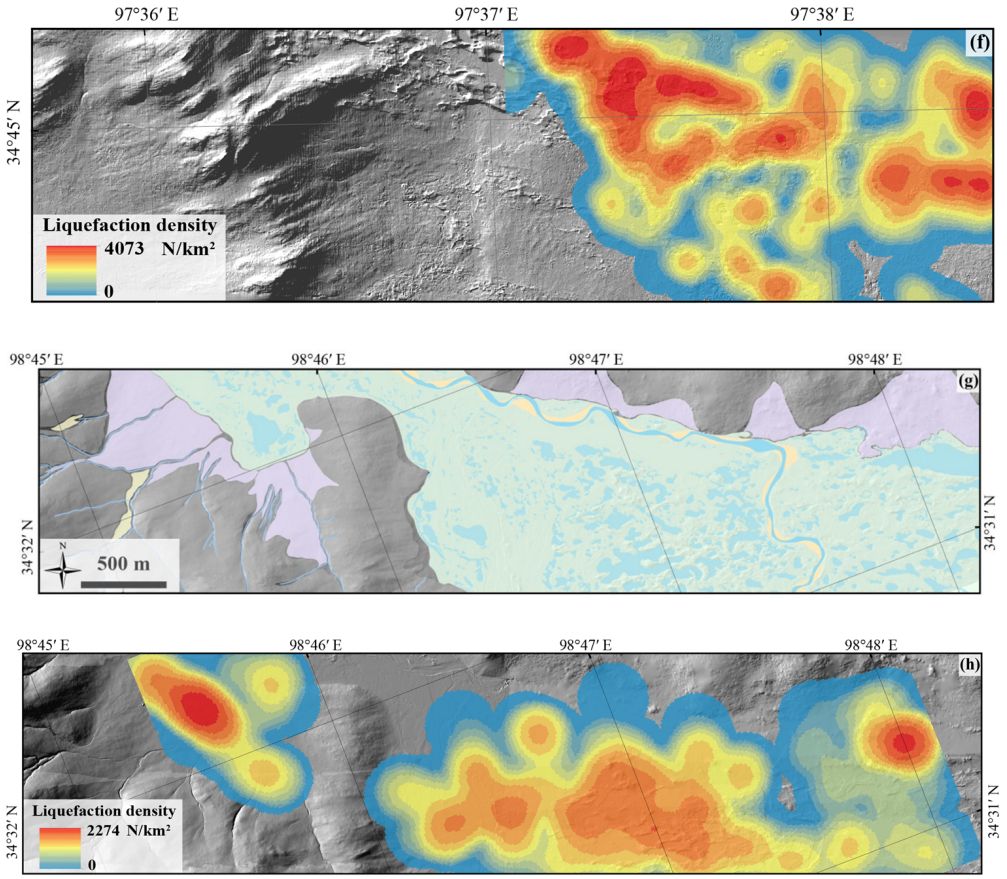

Figure 9. Distribution of liquefaction and depositional environments in W0–5 (**a**,**b**), W30–35 (**c**,**d**) and W70–75 (**e**,**f**) and E35–40 (**g**,**h**) sections.

5. Discussion

5.1. Relationship between Seismic Ground Motion and Liquefaction

More than 90% of the coseismic soil liquefaction caused by the Maduo earthquake occurred in the range of PGA > 0.50 g, and the liquefaction density was significantly higher in the region of seismic intensity >VIII (Figure 5b). The highest liquefaction density was detected in the W30–35 section, which is located at Yematan, the area with the highest intensity (X) of the earthquake (Figures 5 and 6). The liquefaction sites are mostly located in regions of seismic intensity >VIII, such as the 2008 Mw 7.9 Wenchuan earthquake [8,13]. The seismic intensity and PGA are a reflection of the ground motion intensity [5,7,47], and the intensity of the seismic ground motion is considered to be an important driver on the soil liquefication during an earthquake [5,7]. In the area with large PGA and high seismic intensity, the ground motion with relatively high amplitude and intensity caused the pore water pressure in the saturated sediment soil to rise abruptly, the force between the soil grains disappeared and, thus, liquefaction was induced [50]. Furthermore, among the seismic shaking-related features, no or very few coseismic landslides occurred during the Maduo earthquake. This is an unusual situation that suggests that the minimum shaking duration requirements, shaking levels, and ground motion intensity for liquefaction may be much lower than that to trigger landslides during the Maduo earthquake.

We also observed that liquefaction is denser in places such as surface rupture step-overs, bends or branching, such as in the W48–50, W23–25 and W5–7 sections of the study area (Figures 1c and 6a). This indicated that a higher amplitude of seismic waves were emitted at fault geometrical complexities. The amplification of seismic waves can cause more complex fracture deformation and greater formation disturbance [8], which leads to increased liquefaction occurrence in these areas. However, we noted that locations of the highest density occurred at ~30 km west of the epicenter. In terms of the location along

the rupture, it was not a place with geometrical complexities, such as step-overs or fault bends. However, detailed investigation showed that it was at the transition zone from the scattered surface ruptures in the east to the continuous traces of prominent moletracks and fault scarps to the west. We speculated that the peak density of the liquefaction here may indicate that the west propagating rupture started to surface and enhanced the surface fissuring, fault damage and ground motion.

Although the earthquake miraculously caused no fatalities, the strong shaking still caused serious damage to public facilities, and the Yematan Bridge was the most severely damaged area of the event. Several articles have reported and analyzed the causes of the bridge's severe damage: it was very close to the broad surface rupture zone and the seismic intensity impact reached X in this region, with extremely violent ground shaking [4,5]. Our field investigation revealed that there was significant coseismic liquefaction near the bridge, and the statistical results also showed that section W30–35, corresponding to the Yematan Bridge, had the highest liquefaction density. In almost every strong earthquake, widespread coseismic liquefaction induced ground deformation and subsidence could cause intense damage to infrastructures and engineering structures [7,8]. Thus, it is possible that severe liquefaction exacerbated the damage in the area.

Moreover, we found that the site of the highest density of liquefaction was not inside the highest PGA area, but was rather a moderate-high area (0.50–0.60 g). Several factors, which are related to the seismic parameters, the site conditions, and the soil properties, control the liquefaction generation and distribution [51]. In the zone of PGA with values 0.50–0.60 g, it had a very high liquefaction density near 0 km (correspond to the epicenter) (Figure 5a,b). Liquefaction is more likely to be induced by higher and more complex radiated waves at the initiation phase of the earthquake rupture [50]. In addition, the depositional environment in the area is the Yellow River floodplain, with a high groundwater level and sediment particles of mostly fine sand and clay, which makes it more favorable for liquefaction generation. The massive liquefaction near 0 km increased the liquefaction density in the 0.50–0.60 g section.

5.2. Liquefaction Density Decay with Distance from the Surface Rupture

We detected that the liquefaction density was the highest in the vicinity of the surface rupture and maintained a high level within 250 m of the rupture. Then, the liquefaction density decreased in an inverse power law with the increasing distance (Figure 7). The same regulation was found in studies of coseismic landslides. Bloom et al. [52] found that the coseismic landslide density decreases with the increasing distance from the fault in the 2016 Mw 7.8 Kaikōura earthquake. This phenomenon was attributed to the fact that the ground motion is more intense near the fault, while the ground motion weakens with the increasing distance from the fault [52]. In this study, the decline of the liquefaction density with the distance from the rupture could be due to a similar mechanism. Furthermore, Rodriguez Padilla et al. [49] found that the strain intensity also declined with the inverse power law along with the fault normal distance and the aftershock density. They attributed the intense near-fault damage to the coseismic fracturing. Thus, the higher liquefaction density near the rupture zone could be due to stronger ground motions and more intense ground deformation of the locations closer to the rupture [53,54], or decreased material strength (shear) caused by the coseismic rupture damage effect [49].

No such threshold has been observed throughout the previous studies on coseismic liquefaction. We inferred that the numerical size of the threshold may be related to the width of the rupture damage zone. Within the fault damage zone, it usually contain fractures, fractured rocks, and fluids, and seismic wave velocity would decreases within it [55,56]. The periphery of the rupture zone is surrounded by wall rocks with relatively high seismic wave velocities [57,58], and the seismic waves trapped within it may be amplified. Therefore, the liquefaction density was at a high level within the rupture damage zone. In addition, when the rupture zone is covered by loose sediments, the amplification effect of seismic waves may be even stronger [58]. The amplification of the seismic wave vibrations

in the vicinity of the rupture zone could explain the enhancement of the liquefaction effects near it.

It is interesting to observe that the liquefaction density saturates within a 250 m width of the surface rupture, which is reported for the first time. Thanks to the cm-resolution UAV images, we could map the liquefaction sites in unprecedent detail. However, the databases used in our study are concentrated within 1.5 km near the rupture and the total length of the study area is ~160 km. The study area do not contain liquefaction sites outside the swath corridor. For example, Xu et al. [59] pointed out that some liquefaction sites outside the surface rupture as far as 2–10 km away, particularly along the Yellow River in the east of the epicenter. However, the liquefaction density decay function deduced from our 1.5 km-wide near-rupture swath provides a frame to estimate the number of liquefactions in the far field, which should decrease fast perpendicular to the fault. Complete liquefaction investigations could help enrich the globe database of coseismic liquefaction, and a future study should include a larger area to constrain a more complete distribution of liquefaction induced by the earthquakes. Currently, automatic identification of coseismic surface rupture and liquefaction based on machine learning methods, which relies on satellite or aerial imagery and can cover a wider area, is gradually applied [60–62]. And the accuracy of recognition of coseismic liquefaction can reach 90% within the small test area [62]. However, this method requires very high image resolution, otherwise it is difficult to identify liquefaction sites. Moreover, the method is still vague on the criteria of liquefaction identification, and could falsely assign animal burrows as liquefaction pits. Therefore, in order to comprehensively and truly reflect the coseismic liquefaction characteristics, future investigations of liquefaction need to be carried out by a combination of multiple methods.

5.3. Influence of the Sedimentary Environment

In our study, the coseismic liquefaction was concentrated in the W0–5, W20–35, W70–75, E0–5, and E35–50 sections (Figures 5 and 6), and we have identified that these sections correspond to the area on the south side of the Eling Lake, the Yellow River floodplain, and the Heihe River floodplain. Liquefaction induced by earthquakes worldwide is more likely to occur near rivers, lakes, lagoons, or coastal areas [10], also shown in other cases, including the Canterbury earthquake sequence (New Zealand) [7,15], the Ridgecrest earthquake (USA) [16], the Durrës Earthquake (Albania) [63], and the Wenchuan earthquake (China) [8,11,12]. These studies, as well as ours, support that the favorable environment for liquefaction include saturated and/or very shallow water tables and loose, fine-grained sandy sediments, and a less permeable top clay-rich sediment cover [63,64].

Within a 1.5 km width of the surface rupture, a significant difference in the liquefaction distribution between the east and west of the epicenter occurred (Figures 5 and 6). The proportion of liquefaction on the west side was much higher (86.87%) than the east side. The liquefaction distribution was also highly asymmetric on both sides of the epicenter in the Arequipa 2001 earthquake. A previous study proposed that the surface rupture was unilateral in propagation in the Arequipa earthquake, and thus the energy release and the shaking duration increased gradually along the propagation direction, leading to the difference in the liquefaction distribution [65]. However, this explanation does not apply to the Maduo earthquake because both sides of the epicenter have high PGA, as well as seismic intensity, such as the E55–60 and E80–84 sections (Figures 5 and 6). We found that the spatial distribution of the earthquake-triggered liquefaction is closely related to the specific sedimentary environment. Within our study area, the west side is dominated by Quaternary (Holocene) alluvial, flood, and lacustrine deposits, and rivers, lakes, and swamps are widely distributed. The local sedimentary environments with loose sand and a high groundwater level provide the ideal preconditions for the large-scale occurrence of liquefaction. In contrast, Mesozoic bedrocks dominate the geology on the east side of the epicenter, such as E12–32 and E77–84 sections (Figure 6). Therefore, liquefaction is hampered in this region.

According to the global seismic liquefaction sensitivity model proposed by Zhu et al. [66], the USGS (https://earthquake.usgs.gov/earthquakes, accessed on 22 May 2021) mapped the liquefaction sensitivity distribution of the Maduo earthquake (Figure 10a). The map showed that the liquefaction susceptibility was higher in the areas flowing through the Yellow River and the Heihe River, as well as near the Eling Lake and the Dongcaoalong Lake, which was consistent with the results of our study. However, the USGS map was a preliminary estimate provided immediately after the earthquake and many of the parameters were not accurately corrected later, such as the soil saturation, sediment distribution, and seismic parameters, such as PGA, PGV, and earthquake duration. We compared the liquefaction susceptibility and the liquefaction density in the 10–35 km section west of epicenter (W10–35) (Figure 10b,c), and found that the distributions of the two were in good agreement near the rupture zone. But compared with the density decay function parameter fit given in our study (Figure 10d), the high value kilometers from the fault is still over-predicted in the USGS map. The predicted high values are mostly along major river floodplains; the USGS map may underestimate the fast decay of ground motion or seismic intensity with distance. Our study provides detailed mapping of coseismic liquefaction at high altitudes, an under-represented environment in the current world liquefaction database, and the results will provide valuable data support for the establishment of more accurate liquefaction prediction models in the future.

Our results show that under the geological conditions of loose sedimentary materials and a high water table, such as the Yellow River source area, once a strong earthquake occurs, it is very likely to induce large-scale coseismic soil liquefaction. Therefore, the construction of public facilities in such areas, including houses, bridges, and roads, need to be planned more carefully. Alternatively, such a large scale of coseismic liquefaction is bound to aggravate a negative impact on the local ecology, just as the coseismic liquefaction destroyed the meadow vegetation and transported loose sandy sediments to the surface, which may provide sources for desertification in this region. Under the background of permafrost degradation due to global warming, the protection of the ecological environment in the Sanjiangyuan region (it consists of the source regions of three large rivers: the Yangtze, the Yellow River, and the Lancang-Mekong) becomes particularly important. We should pay more attention to earthquake risk and coseismic liquefaction damage in these regions, and both natural damage and human activities should be reduced.

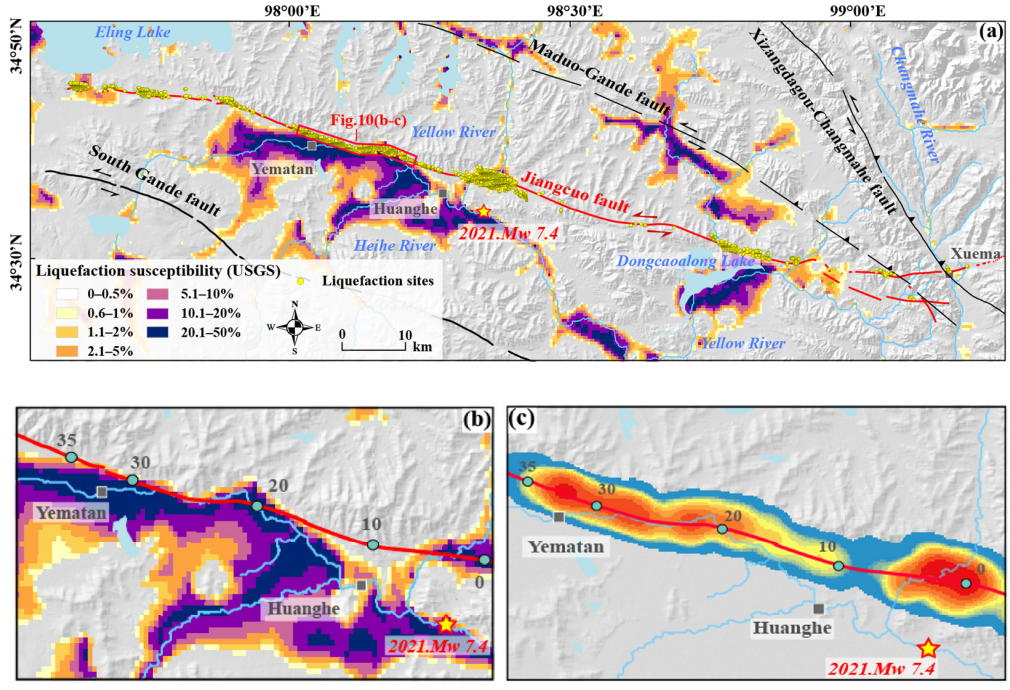

Figure 10. *Cont.*

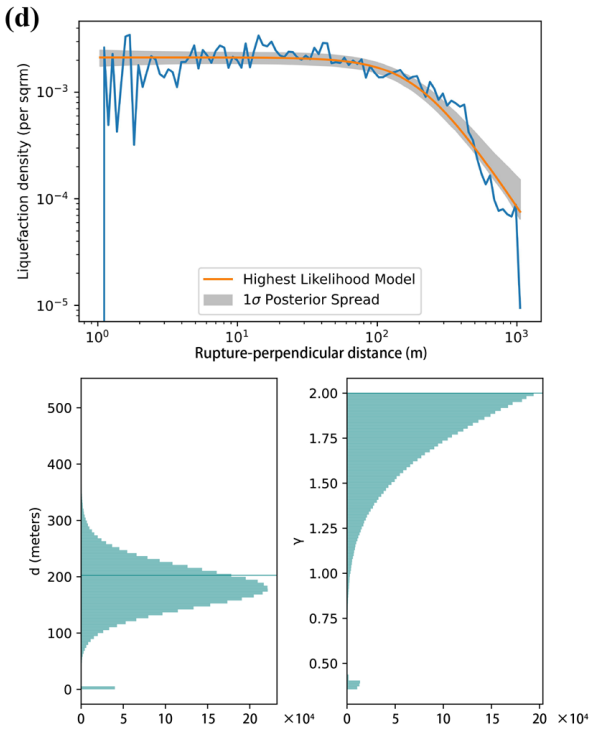

Figure 10. (**a**) The liquefaction susceptibility map of the Maduo Mw 7.4 earthquake, modified by the USGS (https://earthquake.usgs.gov/earthquakes, accessed on 22 May 2021). The yellow points are the coseismic soil liquefaction datasets interpreted based on UAV images. Small red box is location of Figure 10b,c. (**b**) The liquefaction susceptibility distribution in the 10–35 km section west of epicenter (W10–35). (**c**) Density distribution map of coseismic soil liquefaction in W10–35 (from Figure 5b). (**d**) Variation of liquefaction density with increasing distance from the surface rupture in W10–35.

6. Conclusions

In this study, we obtain the Digital Orthophoto Maps (DOMs) within a 1.5 km width along the coseismic surface rupture of the Maduo earthquake using UAV photogrammetry technology. The manual identification and fine mapping of soil liquefaction are completed by these DOMs to investigate the distribution characteristics and influencing factors of coseismic liquefaction.

The association among the distance from the surface rupture, the peak ground acceleration (PGA), seismic intensity and the occurrence of liquefaction reveal that the seismic ground motion was an important controller of coseismic liquefaction during the Maduo earthquake. The coseismic liquefaction density remained on a higher level within 250 m from the rupture, then it declined inversely with the increasing distance in the power law further away from the rupture, and the amplification of the seismic wave vibrations in the vicinity of the rupture zone enhanced the coseismic liquefaction effects near it. More than 90% of the coseismic soil liquefaction occurred in PGA > 0.50 g, and the liquefaction density was significantly higher in the intensity > VIII region.

The sedimentary environment had a great influence on the distribution of the coseismic liquefaction. Liquefaction occurred more frequently in the lake/swamp deposits and fluvial deposits, accounting for 54.78% and 32.95%, respectively, and rarely occurred in bedrocks. Within our 1.5 km-wide near-rupture swath, the proportion of liquefaction on the west side of the epicenter was much higher (86.87%) than on the east side. This difference is related to the depositional environments in the research corridor: where loose Quaternary sediments are widely distributed in the west, predominantly Mesozoic bedrocks are exposed in the east. Sedimentary environments with saturated loose fine-grained sandy soil and a high water table, such as the Eling Lake section and the floodplain area where the Yellow River and Heihe River are located, are more susceptible to the induction of coseismic liquefaction.

Using the cm-resolution UAV images, we were able to map the liquefaction sites in unprecedented detail. Limited by the UAV coverage, our data only covers a 1.5 km-wide swath, which is narrower than the liquefaction affected region in this earthquake, but it is systematic along the entire coseismic surface rupture zone. This study presents the detailed mapping of coseismic liquefaction at high altitudes and in alpine desert grassland regions and provides valuable data support for liquefaction prediction models and seismic hazard assessment.

Author Contributions: Conceptualization, W.W. (Wenxin Wang) and J.L.-Z.; methodology, W.W. (Wenxin Wang), Y.S., L.H. and X.L.; validation, W.W. (Wenxin Wang), J.L.-Z., Y.S., L.H. and W.Y.; formal analysis, W.W. (Wenxin Wang) and J.L.-Z.; investigation, W.W. (Wenxin Wang), J.L.-Z., Y.S., L.H., W.Y., X.Z., X.L., F.C. and H.T.; data curation, W.W. (Wenxin Wang), Z.W., L.H., X.S., K.Q., Y.G., G.H., X.Z., F.C., Z.L. and J.L.; writing—original draft preparation, W.W. (Wenxin Wang); writing—review and editing, W.W. (Wenxin Wang), J.L.-Z., Y.S., L.H., W.Y. and W.W. (Wei Wang); visualization, W.W. (Wenxin Wang), Z.W. and W.Y.; supervision, J.L.-Z. and Y.S.; project administration, J.L.-Z.; funding acquisition, J.L.-Z. All authors have read and agreed to the published version of the manuscript.

Funding: This work was supported by the National Natural Science Foundation of China (U1839203, 42202232, 42272242, 42030305), Central Public-Interest Scientific Institution Basal Research Fund (IGCEA1812), and the State Key Laboratory of Earthquake Dynamic of China (LED2020B03).

Data Availability Statement: Seismic data was obtained from Chinese Earthquake Networks Center (CENC; https://news.ceic.ac.cn/index.html, accessed on 22 May 2021), Ministry of Emergency Management of the People's Republic of China (https://www.mem.gov.cn/xw/yjglbgzdt/202105/t20210528_386251.shtml, accessed on 28 May 2021) and the U.S. Geological Survey (USGS; https://earthquake.usgs.gov/earthquakes/eventpage/us6000ah9t, accessed on 22 May 2021).

Acknowledgments: We would like to thank the UAV vendor for supporting this research with equipment, Alba Rodriguez Padilla for providing the code for calculating the decay of liquefaction density, and Dun Wang for providing the peak ground acceleration (PGA) data to us. We thank Yueren Xu for constructive reviews that improve the quality of the paper. We are also grateful to several anonymous reviewers for their helpful comments and suggestions on this paper.

Conflicts of Interest: The authors declare no conflict of interest.

References

1. Liu-Zeng, J.; Yao, W.; Liu, X.; Shao, Y.; Wang, W.; Han, L.; Wang, Y.; Zeng, X.; Li, J.; Wang, Z.; et al. High-resolution structure-from-motion models covering 160 km-long surface ruptures of the 2021 Mw7.4 Madoi earthquake in northern Qinghai-Tibetan Plateau. *Earthq. Res. Adv.* **2022**, *2*, 100140. [CrossRef]
2. Pan, J.; Li, H.; Chevalier, M.-L.; Tapponnier, P.; Bai, M.; Li, C.; Liu, F.; Liu, D.; Wu, K.; Wang, P.; et al. Coseismic rupture of the 2021, M7.4 Maduo earthquake (northern Tibet): Short-cutting of the Kunlun fault big bend. *Earth Planet. Sci. Lett.* **2022**, *594*, 117703. [CrossRef]
3. Guo, J. Sand liquefaction during the 2021 M7.4 Maduo earthquake, China. *Nat. Hazards* **2022**, *114*, 3359–3375. [CrossRef]
4. Xu, Y.; Zhang, Y.; Liu, R.; Li, W.; Zhang, W.; Du, P.; Tian, Q. Preliminary analyses of landslides and sand liquefaction triggered by 22 May, 2021, Maduo Mw7.3 earthquake on Northern Tibetan Plateau, China. *Landslides* **2022**, *19*, 155–164. [CrossRef]
5. Yuan, J.; Wang, Y.; Zhan, B.; Yuan, X.; Wu, X.; Ma, J. Comprehensive investigation and analysis of liquefaction damage caused by the Ms7.4 Maduo earthquake in 2021 on the Tibetan Plateau, China. *Soil Dyn. Earthq. Eng.* **2022**, *155*, 107191. [CrossRef]
6. Harp, E.L.; Jibson, R.W.; Kayen, R.E.; Keefer, D.K.; Sherrod, B.L.; Carver, G.A.; Collins, B.D.; Moss, R.E.S.; Sitar, N. Landslides and liquefaction triggered by the M7.9 Denali Fault earthquake of 3 November 2002. *GSA Today* **2003**, *13*, 4–10. [CrossRef]
7. Quigley, M.C.; Bastin, S.; Bradley, B.A. Recurrent liquefaction in Christchurch, New Zealand, during the Canterbury earthquake sequence. *Geology* **2013**, *41*, 419–422. [CrossRef]
8. Liu-Zeng, J.; Wang, P.; Zhang, Z.; Li, Z.; Cao, Z.; Zhang, J.; Yuan, X.; Wang, W.; Xing, X. Liquefaction in western Sichuan Basin during the 2008 Mw7.9 Wenchuan earthquake, China. *Tectonophysics* **2017**, *694*, 214–238. [CrossRef]
9. Yao, Y.; Chen, J.; Li, T.; Fu, B.; Wang, H.; Li, Y.; Jia, H. Soil liquefaction in seasonally frozen ground during the 2016 Mw6.6 Akto earthquake. *Soil Dyn. Earthq. Eng.* **2019**, *117*, 138–148. [CrossRef]
10. Huang, Y.; Yu, M. Chapter 2: Macroscopic characteristics of seismic liquefaction. In *Hazard Analysis of Seismic Soil Liquefaction*; Springer Natural Hazards; Springer: Singapore, 2017. [CrossRef]
11. Elgamal, A.W.; Zeghal, M.; Parra, E. Liquefaction of reclaimed island in Kobe, Japan. *J. Geotech. Eng.* **1996**, *122*, 39–49. [CrossRef]
12. Wang, C.Y.; Dreger, D.S.; Wang, C.H.; Mayeri, D.; Berryman, J.G. Field relations among coseismic ground motion, water level change and liquefaction for the 1999 Chi-Chi (Mw = 7.5) earthquake, Taiwan. *Geophys. Res. Lett.* **2003**, *30*, 1890. [CrossRef]

13. Chen, L.; Yuan, X.; Cao, Z.; Hou, L.; Sun, R.; Dong, L.; Wang, W.; Meng, F.; Chen, H. Liquefaction macrophenomena in the great Wenchuan earthquake. *Earthq. Eng. Eng. Vib.* **2009**, *8*, 219–229. [CrossRef]
14. Cao, Z.; Leslie Youd, T.; Yuan, X. Gravelly soils that liquefied during 2008 Wenchuan, China earthquake, Ms = 8.0. *Soil Dyn. Earthq. Eng.* **2011**, *31*, 1132–1143. [CrossRef]
15. Cubrinovski, M.; Bray, J.D.; Taylor, M.; Giorgini, S.; Bradley, B.; Wotherspoon, L.; Zupan, J. Soil liquefaction effects in the central business district during the February 2011 Christchurch earthquake. *Seismol. Res. Lett.* **2011**, *82*, 893–904. [CrossRef]
16. Orense, R.P.; Kiyota, T.; Yamada, S.; Cubrinovski, M.; Hosono, Y.; Okamura, M.; Yasuda, S. Comparison of liquefaction features observed during the 2010 and 2011 Canterbury earthquakes. *Seismol. Res. Lett.* **2011**, *82*, 905–918. [CrossRef]
17. Villamor, P.; Almond, P.; Tuttle, M.P.; Giona-Bucci, M.; Langridge, R.M.; Clark, K.; Ries, W.; Bastin, S.H.; Eger, A.; Vandergoes, M.; et al. Liquefaction features produced by the 2010–2011 Canterbury earthquake sequence in southwest Christchurch, New Zealand, and preliminary sssessment of paleoliquefaction features. *Bull. Seismol. Soc. Am.* **2016**, *106*, 1747–1771. [CrossRef]
18. Zimmaro, P.; Nweke, C.C.; Hernandez, J.L.; Hudson, K.S.; Hudson, M.B.; Ahdi, S.K.; Boggs, M.L.; Davis, C.A.; Goulet, C.A.; Brandenberg, S.J.; et al. Liquefaction and related ground failure from July 2019 Ridgecrest earthquake sequence. *Bull. Seismol. Soc. Am.* **2020**, *110*, 1549–1566. [CrossRef]
19. Yi, Z.; Buckreis, T.; Issa, O.; Yeung, J.S.; Lyda, A.; Gallien, T.W.; Kim, Y.; Lucey, J.; Delisle, M.-P.; Winters, M.A.; et al. Ground deformation data from GEER investigations of Ridgecrest earthquake sequence. *Seismol. Res. Lett.* **2020**, *91*, 2024–2034. [CrossRef]
20. Fu, S.; Tatsuoka, F. Soil liquefaction during Haicheng and Tangshan earthquake in China; a review. *Soils Found.* **1984**, *24*, 11–29. [CrossRef]
21. Owen, G.; Moretti, M. Identifying triggers for liquefaction-induced soft-sediment deformation in sands. *Sediment. Geol.* **2011**, *235*, 141–147. [CrossRef]
22. Westoby, M.J.; Brasington, J.; Glasser, N.F.; Hambrey, M.J.; Reynolds, J.M. 'Structure-from-Motion' photogrammetry: A low-cost, effective tool for geoscience applications. *Geomorphology* **2012**, *179*, 300–314. [CrossRef]
23. Fonstad, M.A.; Dietrich, J.T.; Courville, B.C.; Jensen, J.L.; Carbonneau, P.E. Topographic structure from motion: A new development in photogrammetric measurement. *Earth Surf. Process Landf.* **2013**, *38*, 421–430. [CrossRef]
24. Bi, H.; Zheng, W.; Ren, Z.; Zeng, J.; Yu, J. Using an unmanned aerial vehicle for topography mapping of the fault zone based on structure from motion photogrammetry. *Int. J. Remote Sens.* **2016**, *38*, 2495–2510. [CrossRef]
25. Javernick, L.; Brasington, J.; Caruso, B. Modeling the topography of shallow braided rivers using Structure-from-Motion photogrammetry. *Geomorphology* **2014**, *213*, 166–182. [CrossRef]
26. Franke, K.W.; Rollins, K.M.; Ledezma, C.; Hedengren, J.D.; Wolfe, D.; Ruggles, S.; Bender, C.; Reimschiissel, B. Reconnaissance of two liquefaction sites using small unmanned aerial vehicles and structure from motion computer vision following the April 1, 2014 Chile earthquake. *J. Geotech. Geoenviron.* **2017**, *143*. [CrossRef]
27. Papathanassiou, G.; Valkaniotis, S.; Pavlides, S. The July 20, 2017 Bodrum-Kos, Aegean Sea Mw = 6.6 earthquake; preliminary field observations and image-based survey on a lateral spreading site. *Soil Dyn. Earthq. Eng.* **2019**, *116*, 668–680. [CrossRef]
28. Tapponnier, P.; Peltzer, G.; Le Dain, A.Y.; Armijo, R.; Cobbold, P. Propagating extrusion tectonics in Asia: New insights from simple experiments with plasticine. *Geology* **1982**, *10*, 611–616. [CrossRef]
29. Rui, X.; Stamps, D.S. Present-day kinematics of the eastern Tibetan Plateau and Sichuan Basin: Implications for lower crustal rheology. *J. Geophys. Res. Solid Earth* **2016**, *121*, 3846–3866. [CrossRef]
30. Burchfiel, B.C.; Zhiliang, C.; Yupinc, L.; Royden, L.H. Tectonics of the Longmen Shan and adjacent regions, central China. *Int. Geol. Rev.* **2010**, *37*, 661–735. [CrossRef]
31. Klinger, Y.; Xu, X.; Tapponnier, P.; Van der Woerd, J.r.; Lasserre, C.; King, G. High-resolution satellite imagery mapping of the surface rupture and slip distribution of the Mw~7.8, 14 November 2001 Kokoxili earthquake, Kunlun fault, northern Tibet, China. *Bull. Seismol. Soc. Am.* **2005**, *95*, 1970–1987. [CrossRef]
32. Liu-Zeng, J.; Zhang, Z.; Wen, L.; Tapponnier, P.; Sun, J.; Xing, X.; Hu, G.; Xu, Q.; Zeng, L.; Ding, L.; et al. coseismic ruptures of the 12 May 2008, Ms8.0 Wenchuan earthquake, Sichuan: East–west crustal shortening on oblique, parallel thrusts along the eastern edge of Tibet. *Earth Planet. Sci. Lett.* **2009**, *286*, 355–370. [CrossRef]
33. Xu, C.; Xu, X.; Lee, Y.H.; Tan, X.; Yu, G.; Dai, F. The 2010 Yushu earthquake triggered landslide hazard mapping using GIS and weight of evidence modeling. *Environ. Earth Sci.* **2012**, *66*, 1603–1616. [CrossRef]
34. Xu, X.; Wen, X.; Han, Z.; Chen, G.; Li, C.; Zheng, W.; Zhnag, S.; Ren, Z.; Xu, C.; Tan, X.; et al. Lushan Ms7.0 earthquake: A blind reserve-fault event. *Chin. Sci. Bull.* **2013**, *58*, 3437–3443. [CrossRef]
35. Xu, X.; Tan, X.; Yu, G.; Wu, G.; Fang, W.; Chen, J.; Song, H.; Shen, J. Normal- and oblique-slip of the 2008 Yutian earthquake: Evidence for eastward block motion, northern Tibetan Plateau. *Tectonophysics* **2013**, *584*, 152–165. [CrossRef]
36. Yuan, Z.; Liu-Zeng, J.; Li, X.; Xu, J.; Yao, W.; Han, L.; Li, T. Detailed mapping of the surface rupture of the 12 February 2014 Yutian Ms7.3 earthquake, Altyn Tagh fault, Xinjiang, China. *Sci. China Earth Sci.* **2020**, *64*, 127–147. [CrossRef]
37. Sun, J.; Yue, H.; Shen, Z.; Fang, L.; Zhan, Y.; Sun, X. The 2017 Jiuzhaigou earthquake: A complicated event occurred in a young fault system. *Geophys. Res. Lett.* **2018**, *45*, 2230–2240. [CrossRef]

38. Tapponnier, P.; Xu, Z.; Roger, F.; Meyer, B.; Arnaud, N.; Wittlinger, G.; Yang, J. Oblique stepwise rise and growth of the Tibet Plateau. *Science* **2001**, *294*, 1671–1677. [CrossRef] [PubMed]
39. Ren, J.; Xu, X.; Zhang, G.; Wang, Q.; Zhang, Z.; Gai, H.; Kang, W. Coseismic surface ruptures, slip distribution, and 3D seismogenic fault for the 2021 Mw7.3 Maduo earthquake, central Tibetan Plateau, and its tectonic implications. *Tectonophysics* **2022**, *827*, 229275. [CrossRef]
40. Yuan, Z.; Li, T.; Su, P.; Sun, H.; Ha, G.; Guo, P.; Chen, G.; Thompson Jobe, J. Large surface-rupture gaps and low surface fault slip of the 2021 Mw7.4 Maduo earthquake along a low-activity strike-slip fault, Tibetan Plateau. *Geophys. Res. Lett.* **2022**, *49*, e2021GL096874. [CrossRef]
41. Liu, X.; Xia, T.; Liu-zeng, J.; Yao, W.; Xu, J.; Deng, D.; Han, L.; Jia, Z.; Shao, Y.; Wang, Y.; et al. Distributed characteristics of the surface deformations associated with the 2021 Mw7.4 Madoi earthquake, Qinghai, China. *Seismol. Geol.* **2022**, *44*, 461–483. (In Chinese) [CrossRef]
42. James, M.R.; Robson, S.; d'Oleire-Oltmanns, S.; Niethammer, U. Optimising UAV topographic surveys processed with structure-from-motion: Ground control quality, quantity and bundle adjustment. *Geomorphology* **2017**, *280*, 51–66. [CrossRef]
43. Turner, D.; Lucieer, A.; Wallace, L. Direct georeferencing of ultrahigh-resolution UAV imagery. *IEEE Trans. Geosci. Remote Sens.* **2014**, *52*, 2738–2745. [CrossRef]
44. Ajayi, O.G.; Salubi, A.A.; Angbas, A.F.; Odigure, M.G. Generation of accurate digital elevation models from UAV acquired low percentage overlapping images. *Int. J. Remote Sens.* **2017**, *38*, 3113–3134. [CrossRef]
45. Giordan, D.; Adams, M.S.; Aicardi, I.; Alicandro, M.; Allasia, P.; Baldo, M.; De Berardinis, P.; Dominici, D.; Godone, D.; Hobbs, P.; et al. The use of unmanned aerial vehicles (UAVs) for engineering geology applications. *Bull. Eng. Geol. Environ.* **2020**, *79*, 3437–3481. [CrossRef]
46. Nex, F.; Remondino, F. UAV for 3D mapping applications: A review. *Appl. Geomat.* **2013**, *6*, 1–15. [CrossRef]
47. Chen, W.; Wang, D.; Zhang, C.; Yao, Q.; Si, H. Estimating seismic intensity maps of the 2021 Mw7.3 Madoi, Qinghai and Mw6.1 Yangbi, Yunnan, China earthquakes. *J. Earth Sci.* **2022**, *33*, 839–846. [CrossRef]
48. Powers, P.M.; Jordan, T.H. Distribution of seismicity across strike-slip faults in California. *J. Geophys. Res.* **2010**, *115*. [CrossRef]
49. Rodriguez Padilla, A.M.; Oskin, M.E.; Milliner, C.W.D.; Plesch, A. Accrual of widespread rock damage from the 2019 Ridgecrest earthquakes. *Nat. Geosci.* **2022**, *15*, 222–226. [CrossRef]
50. Huang, Y.; Yu, M. Review of soil liquefaction characteristics during major earthquakes of the twenty-first century. *Nat. Hazards* **2012**, *65*, 2375–2384. [CrossRef]
51. Tang, X.W.; Hu, J.L.; Qiu, J.N. Identifying significant influence factors of seismic soil liquefaction and analyzing their structural relationship. *KSCE J. Civ. Eng.* **2016**, *20*, 2655–2663. [CrossRef]
52. Bloom, C.K.; Howell, A.; Stahl, T.; Massey, C.; Singeisen, C. The influence of off-fault deformation zones on the near-fault distribution of coseismic landslides. *Geology* **2022**, *50*, 272–277. [CrossRef]
53. Chen, H.; Qu, C.; Zhao, D.; Ma, C.; Shan, X. Rupture kinematics and coseismic slip model of the 2021 Mw7.3 Maduo (China) earthquake: Implications for the seismic hazard of the Kunlun fault. *Remote Sens.* **2021**, *13*, 3327. [CrossRef]
54. Zhao, D.; Qu, C.; Chen, H.; Shan, X.; Song, X.; Gong, W. Tectonic and geometric control on fault kinematics of the 2021 Mw7.3 Maduo (China) earthquake inferred from interseismic, coseismic, and postseismic InSAR observations. *Geophys. Res. Lett.* **2021**, *48*, e2021GL095417. [CrossRef]
55. Chester, F.M.; Chester, J.S. Ultracataclasite structure and friction processes of the Punchbowl fault, San Andreas system, California. *Tectonophysics* **1998**, *295*, 199–221. [CrossRef]
56. Ben-Zion, Y.; Sammis, C.G. Characterization of fault zones. *Pure Appl. Geophys.* **2003**, *160*, 677–715. [CrossRef]
57. Li, Y.G.; Leary, P.C. Fault zone trapped seismic wave. *Bull. Seismol. Soc. Am.* **1990**, *80*, 1245–1271. [CrossRef]
58. Donati, S.; Marra, F.; Rovelli, A. Damage and ground shaking in the town of Nocera Umbra during Umbria-Marche, central Italy, earthquakes: The special effect of a fault zone. *Bull. Seismol. Soc. Am.* **2001**, *91*, 511–519. [CrossRef]
59. Xu, Y.; Zhang, F.; Li, T.; Allen, M.; Yuan, Z.; Li, Z.; Hong, S.; Zhang, Y.; Yuan, X.; Liu, R.; et al. Links between landscapes, seismicity and hydrology revealed by 2021 Maduo Mw7.3 earthquake. *Commun. Earth Environ.* 2023; under review.
60. Zeng, X.; Liu-zeng, J.; Wang, W.; Yao, W.; Wu, J.; Liu, X.; Han, L.; Wang, W.; Xing, Y.; Du, R.; et al. Machine learning in identifyng and mapping the surface rupture of the 2021 Mw7.4 Madoi earthquake, Qinghai. *Chinese J. Geophys.* **2023**, *66*. (In Chinese) [CrossRef]
61. Rashidian, V.; Baise, L.G.; Koch, M. Using high resolution optical imagery to detect earthquake-induced liquefaction: The 2011 Christchurch earthquake. *Remote Sens.* **2020**, *12*, 377. [CrossRef]
62. Liang, P.; Xu, Y.; Li, W.; Zhang, Y.; Tian, Q. Automatic identification of liquefaction induced by 2021 Maduo Mw7.3 earthquake based on machine learning methods. *Remote Sens.* **2022**, *14*, 5595. [CrossRef]
63. Mavroulis, S.; Lekkas, E.; Carydis, P. Liquefaction phenomena induced by the 26 November 2019, Mw = 6.4 Durrës (Albania) earthquake and liquefaction susceptibility assessment in the affected area. *Geosciences* **2021**, *11*, 215. [CrossRef]
64. Papathanassiou, G.; Valkaniotis, S.; Ganas, A.; Stampolidis, A.; Rapti, D.; Caputo, R. Floodplain evolution and its influence on liquefaction clustering: The case study of March 2021 Thessaly, Greece, seismic sequence. *Eng. Geol.* **2022**, *298*, 106542. [CrossRef]

65. Audemard, M.F.A.; Gómez, J.C.; Tavera, H.J.; Orihuela, N. Soil liquefaction during the Arequipa Mw8.4, June 23, 2001 earthquake, southern coastal Peru. *Eng. Geol.* **2005**, *78*, 237–255. [CrossRef]
66. Zhu, J.; Baise, L.G.; Thompson, E.M. An updated geospatial liquefaction model for global application. *Bull. Seismol. Soc. Am.* **2017**, *107*, 1365–1385. [CrossRef]